Research Square

Preprints are preliminary reports that have not undergone peer review.
They should not be considered conclusive, used to inform clinical practice,
or referenced by the media as validated information.

Effect of Pulse-Duration Ratio on Microstructural Evolution, Mechanical Properties, Phase Transformation, and Corrosion Resistance of Autogenously DPTIG-Welded Nitinol Sheets

Manoj Samson R

manoj.sam6@gmail.com

SRM Institute of Science and Technology: SRM Institute of Science and Technology (Deemed to be University)

Saravanakumar R

SRM Institute of Science and Technology: SRM Institute of Science and Technology (Deemed to be University)

Sanjeev Kumar

SRM Institute of Science and Technology - Delhi NCR Campus

Chandan Pandey

IIT Jodhpur: Indian Institute of Technology Jodhpur

Research Article

Keywords: NiTinol, Double pulse TIG Welding, Characterization, Tensile Strength, Corrosion resistance

Posted Date: November 13th, 2026

DOI: https://doi.org/10.21203/rs.3.rs-11376218/v1

License: This work is licensed under a Creative Commons Attribution 4.0 International License.
Read Full License

Effect of Pulse-Duration Ratio on Microstructural Evolution, Mechanical Properties, Phase Transformation, and Corrosion Resistance of Autogenously DPTIG-Welded Nitinol Sheets

Manoj Samson R[1*], R Saravanakumar[1], Sanjeev Kumar[2], Chandan Pandey[3]

[1]Department of Mechanical Engineering, SRM Institute of Science and Technology, Kattankulathur, Chengalpattu, Tamil Nadu, India-603203.
[2]Department of Mechanical Engineering, SRM Institute of Science and Technology, Delhi NCR Campus, Modinagar, Uttar Pradesh, 201204, India
[3]Department of Mechanical Engineering, Indian Institute of Technology Jodhpur, Jodhpur, 342030, India

*Corresponding Author: manoj.sam6@gmail.com

Abstract

Joining thin Nitinol sheets remains challenging because the thermal cycles associated with fusion welding can substantially alter their microstructure, mechanical properties, phase transformation behaviour, and corrosion resistance. In this study, 1 mm-thick Nitinol sheets were autogenously welded using double-pulse tungsten inert gas (DPTIG) welding to investigate the effects of pulse-duration ratio on weld bead geometry, microstructure, mechanical properties, phase transformation behaviour, and corrosion performance. Three pulse-duration ratios (50-50%, 40-60%, and 60-40%) were investigated. Full penetration was achieved under all welding conditions, while the 40-60% condition produced the narrowest weld bead and promoted grain refinement. The fusion zone predominantly comprised B2 austenite with columnar grains, alongside the formation of Ti_2Ni and Ni_3Ti intermetallic phases. Among the investigated conditions, the 40-60% ratio yielded the finest average grain size (24 ± 2 μm), the highest high-angle grain boundary (HAGB) fraction (76%), and the highest tensile strength (583 ± 11 MPa), representing an approximately 3% improvement over the 50–50% condition. Differential scanning calorimetry (DSC) revealed the B2-B19′ martensitic transformation, with no discernible R-phase transformation peak. In contrast, the 60-40% condition exhibited the lowest corrosion rate of 0.00402 mm/year. These findings demonstrate that pulse-duration ratio influences weld geometry, microstructural evolution, tensile performance, phase transformation behavior, and corrosion resistance in DPTIG-welded Nitinol sheets, highlighting its potential as a process parameter for tailoring the properties of welded Nitinol components.

Keywords: NiTinol; Double pulse TIG Welding; Characterization; Tensile Strength; Corrosion resistance.

1. Introduction

Nickel-titanium (NiTi), commercially known as Nitinol, is one of the most widely studied shape memory alloys owing to its distinctive functional and mechanical properties. Its reversible martensitic transformation underpins two characteristic behaviours: the shape memory effect (SME), which enables the recovery of a predefined shape upon appropriate thermal stimulation, and superelasticity, which allows substantial recoverable deformation through stress-induced phase transformation. In addition to these functional characteristics, NiTi exhibits high mechanical strength, excellent fatigue resistance, good corrosion resistance, and favourable biocompatibility. This unique combination of properties makes NiTi particularly attractive for applications involving cyclic deformation, functional reliability, and prolonged exposure to demanding service environments [1–3]. Recent studies have further demonstrated the importance of fatigue resistance and microstructural control in determining the long-term functional reliability of NiTi components [4]. The combination of functional properties and biocompatibility has established NiTi as an important material for biomedical applications, including vascular stents, guidewires, orthodontic devices, and other minimally invasive components [1,2]. Its reversible deformation and high work density have also encouraged its use in smart actuators and adaptive structures for aerospace and other engineering applications [3,4]. The increasing application of NiTi in complex and miniaturized components has increased the demand for reliable manufacturing and joining techniques that preserve its distinctive functional properties. Welding is particularly important for assembling thin NiTi sheets and miniature components; however, the thermal cycles associated with fusion welding can significantly alter the weld microstructure, promote the formation of brittle intermetallic phases, and adversely affect the mechanical properties, phase transformation behaviour, and corrosion resistance of the joint. Recent investigations on microwelded NiTi joints have specifically identified intermetallic compound formation and preservation of superelasticity and corrosion performance as important challenges in NiTi joining [6].

The fabrication of Nitinol components using conventional machining techniques remains challenging owing to the alloy's pronounced work-hardening tendency, high ductility, and associated tool-wear mechanisms, which can

reduce machining efficiency and compromise surface integrity [7,8]. Recent studies have demonstrated that the machining response of NiTi is strongly influenced by its microstructural characteristics and thermo-mechanical behaviour, contributing to accelerated tool wear and difficulties in achieving the desired surface quality and dimensional accuracy [9,10]. Consequently, reliable joining technologies are essential for manufacturing complex Nitinol structures and assemblies, particularly for miniaturized biomedical components. Recent investigations on NiTi microwelding have demonstrated the importance of controlled joining processes for the fabrication of multifunctional biomedical devices, while also highlighting the challenges associated with intermetallic phase formation and preservation of the functional properties of NiTi [11]. Despite these developments, fusion welding of NiTi remains challenging because the localized thermal cycle can modify the weld microstructure, phase constitution, and functional properties of the alloy. Among the available fusion-welding techniques, laser beam welding (LBW) has attracted considerable attention because its highly concentrated energy source enables localized melting, relatively low heat input, and narrow weld regions. Recent studies on 1 mm-thick Nitinol sheets have demonstrated that laser welding can produce sound joints with controlled weld geometry and favourable mechanical performance while minimizing the extent of thermally affected regions [12].

The functional behavior of Nitinol is governed by reversible phase transformations between the high-temperature austenite phase (B2, body-centered cubic) and the low-temperature martensite phase (B19′, monoclinic). The B2 austenite phase is relatively harder and stronger than the martensitic phase, whereas the latter exhibits higher deformability. Under certain thermal conditions, the phase transformation may proceed through an intermediate rhombohedral (R) phase before transforming into martensite, depending on the alloy composition and thermo-mechanical history [13]. Since the functional properties of NiTi are highly sensitive to microstructural changes, the thermal cycles experienced during welding can significantly influence phase evolution and, consequently, the mechanical and functional performance of the joint. Several researchers have investigated the influence of different welding techniques on the microstructure and properties of NiTi alloys [14]. Delobelle et al. [15] observed a reduction in fusion zone hardness compared with the base material, which was attributed to grain coarsening induced by the welding thermal cycle. Their study also identified welding current as the dominant process parameter governing hardness. Similar observations have been reported for laser-welded NiTi joints, where the fusion zone exhibited lower hardness than the base material despite the formation of relatively narrow fusion and heat-affected zones [16,17].

The formation of brittle intermetallic phases during fusion welding is a major concern for the structural integrity of NiTi joints. In particular, Ti_2Ni and Ni_3Ti phases can compromise mechanical performance by promoting brittleness and reducing load-bearing capacity, while their effects on corrosion resistance depend on their distribution and the resulting microstructural and compositional heterogeneity. Zeng Z et al. [18] reported a marked decrease in the tensile strength of laser-welded NiTi joints with increasing Ti_2Ni precipitate content. Similarly, Falvo et al. [19] observed a 52.72% reduction in tensile strength and a 5% decrease in elongation following laser welding. Oliveira et al. [20] also reported substantial reductions in tensile strength and ductility in TIG-welded annealed NiTi sheets compared with the base material. These findings highlight the influence of welding-induced thermal cycles on microstructural evolution, phase stability, and mechanical performance. Therefore, careful control of welding heat input and thermal history is essential to mitigate microstructural degradation and preserve the functional and mechanical properties of NiTi joints. Several welding techniques have been investigated for joining NiTi alloys, each exhibiting distinct effects on microstructural evolution and joint performance. Kramar et al. [21] compared micro-plasma arc welding (μPAW), laser beam welding (LBW), electron beam welding (EBW), resistance welding, and capacitor discharge welding (CDW) for joining Nitinol. Among the investigated techniques, LBW delivered superior tensile properties, attributed to its relatively low heat input and the associated suppression of brittle intermetallic phase formation. Similarly, the mechanical performance of joints produced by conventional fusion-welding processes is strongly influenced by process parameters, particularly welding current, voltage, and the resulting heat input, which govern the thermal cycle and subsequent microstructural evolution.

In addition to mechanical performance, preserving the phase transformation characteristics of NiTi is essential because they directly govern the shape memory effect and superelastic behavior. Fusion welding often modifies the phase transformation temperatures (PTTs) as a result of localized melting, elemental redistribution, and microstructural changes induced by high thermal input. Consequently, several researchers have investigated solid-state welding processes as an alternative to minimize thermal degradation. Mani Prabhu et al. [22] reported only a marginal variation in the PTT of friction stir welded (FSW) NiTi sheets, while Datta et al. [23] observed the presence of the intermediate R-phase without any significant deterioration of the transformation behavior. In contrast, ultrasonic spot welding with an aluminium interlayer resulted in a more pronounced shift in the transformation temperatures [24]. Similarly, Resnina et al. [25] observed considerable changes in the PTT of wire arc additively manufactured NiTi, primarily due to compositional variations arising from nickel depletion.

Conversely, Manoj Samson et al. [26] demonstrated that optimized TIG welding resulted in relatively smaller deviations in the transformation temperatures compared with several other fusion welding processes.

Corrosion resistance is another critical performance criterion, particularly for biomedical applications where long-term biocompatibility and structural integrity are essential. Previous studies have shown that the corrosion behavior of welded NiTi alloys is closely related to heat input, intermetallic precipitation, and surface oxide stability. Saha et al. [27] reported that laser welding performed under low heat input conditions enhanced corrosion resistance by minimizing microstructural degradation. Likewise, Datta et al. [28] attributed the improved corrosion performance of fiber laser-welded NiTi joints to the formation of a stable TiO_2 passive layer and the reduced precipitation of brittle intermetallic phases associated with lower heat input. Overall, the available literature demonstrates that welding heat input is the dominant factor controlling the microstructure, phase transformation behavior, mechanical properties, and corrosion resistance of NiTi joints. Although low heat input welding processes have shown promising results, achieving an optimum balance between joint strength, phase stability, and corrosion performance remains a significant challenge. Therefore, further investigation into advanced heat input control strategies, such as double-pulse TIG welding, is required to improve the overall performance of welded Nitinol components. A major limitation of laser beam welding is the potential formation of porosity within the fusion zone, which can compromise the mechanical integrity and service performance of NiTi joints. Addressing this issue requires effective control of weld pool dynamics and solidification behaviour. In this context, double-pulse tungsten inert gas (DPTIG) welding offers a promising alternative through periodic modulation of the welding current between peak and base levels, enabling improved control of heat input and weld pool behaviour [29]. The resulting thermal and electromagnetic fluctuations can promote melt circulation through Lorentz forces and Marangoni convection, potentially enhancing elemental homogenization and facilitating the escape of entrapped gas bubbles before solidification. These effects may help reduce porosity and refine the weld microstructure, thereby improving joint quality [30,31].

The increasing demand for miniaturized and high-performance Nitinol components has intensified the need for reliable joining techniques capable of preserving the alloy's functional, mechanical, and corrosion properties. Although laser beam welding has been extensively employed for joining thin NiTi sheets because of its low heat input and superior weld quality, its high equipment and operating costs limit its widespread industrial adoption [32–36]. Alternative joining processes, including friction stir welding, micro-plasma arc welding, electron beam welding, capacitor discharge welding, resistance welding, ultrasonic spot welding, gas metal arc welding, friction welding, and conventional TIG welding, have also been investigated; however, challenges related to heat input control, microstructural degradation, phase transformation characteristics, and joint performance remain unresolved [37–40].

Double-pulse tungsten inert gas (DPTIG) welding offers a promising alternative by enabling control over weld pool dynamics and heat input through periodic current modulation, potentially promoting grain refinement and modifying solidification behaviour [41]. However, to the best of the authors' knowledge, the application of autogenous DPTIG welding to thin Nitinol sheets has not yet been reported. Moreover, the effects of pulse-duration ratio on weld bead geometry, microstructural evolution, grain boundary characteristics, mechanical properties, phase transformation behaviour, and corrosion resistance remain insufficiently explored. To address these gaps, the present study investigates the autogenous DPTIG welding of 1 mm-thick Nitinol sheets using three pulse-duration ratios: 50-50%, 40-60%, and 60-40%. The effects of these ratios on weld bead geometry, microstructure, grain refinement, hardness, tensile properties, phase transformation temperatures, and corrosion behaviour are systematically evaluated. The findings provide insights into the role of pulse-duration ratio in governing weld pool behaviour, microstructural evolution, and joint performance, highlighting the potential of DPTIG welding as an alternative for joining thin Nitinol sheets.

2. Materials and experimental procedure

Commercial cold-rolled Nitinol sheets measuring 60 mm × 30 mm × 1 mm were used as the base material in this study. Before welding, the sheet surfaces were thoroughly cleaned with acetone to remove surface contaminants, including grease and oil, thereby promoting consistent welding conditions. Autogenous butt joints were fabricated using a Kemppi MasterTig 235 ACDC GM welding machine operated in direct-current (DC) mode. High-purity argon was used as the shielding gas at a flow rate of 12 L min^{-1} to minimize atmospheric contamination during welding. The average welding current was maintained at 25 A throughout the experiments.

All welding experiments were performed under ambient laboratory conditions at a temperature of 32 ± 2 °C and a relative humidity of approximately 80%. Previous studies have demonstrated that welding current, arc voltage,

welding speed, shielding gas flow rate, and heat input are the primary factors governing the weld quality and performance of NiTi alloys [25,26]. Accordingly, the welding parameters adopted in the present work were selected based on the available literature while maintaining a low heat input suitable for welding thin Nitinol sheets. To isolate the influence of pulse duration, the welding frequency, arc voltage, shielding gas flow rate, and heating–cooling cycle were kept constant throughout the study. The welding speed was maintained manually by a certified TIG welder to ensure consistent bead formation. The complete welding parameters are summarized in Table 1. The present investigation focuses on the influence of pulse duration on the weld characteristics of autogenous double-pulse TIG (DPTIG) welded Nitinol sheets. In the DPTIG process, the pulse duration determines the proportion of time spent at the peak and base current levels within each welding cycle, thereby influencing heat input, weld pool dynamics, and solidification behavior. To evaluate its effect, three pulse duration ratios, namely 50-50%, 40-60%, and 60-40% (peak current-base current), were employed while maintaining all other process parameters constant. This experimental approach enabled a systematic assessment of the influence of pulse duration on weld bead geometry, microstructural evolution, mechanical properties, phase transformation temperature, and corrosion behavior.

Table 1 Welding parameters for phase duration

Gas flow rate: 12 L/min, frequency: 2 Hz, and voltage: 8.5V

Pulse Duration (Peak current-Base current)	Average current (A)	Peak current (A)	Base current (A)
50-50%	25	45	10
40-60%	25	45	10
60-40%	25	45	10

I_{avg} was calculated using the formulae shown below

$$I_{avg} = \frac{I_p t_p + I_b t_b}{t_p + t_b} \quad Ampere \tag{1}$$

I_{avg} is the input average current, I_p is peak current, t_p is peak time, I_b is base current, and t_b is background time. The I_{avg} is calculated using equation 1. The welded samples are shown in **Figure 1.**

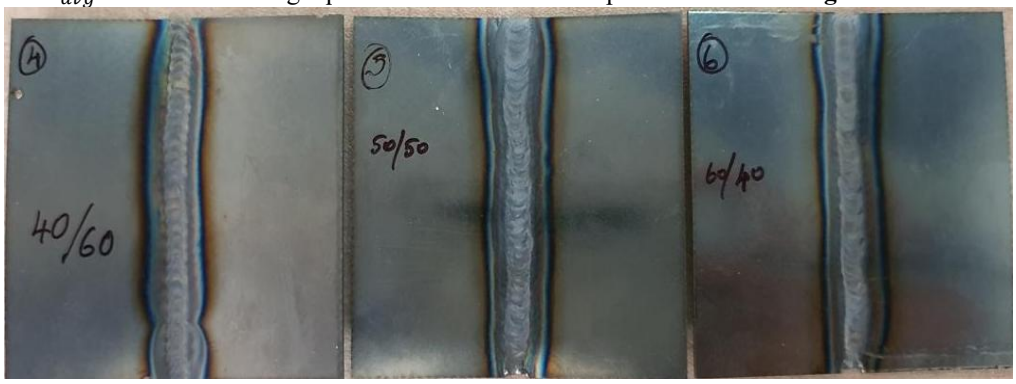


Figure 1. (a-c) Samples welded with change in pulse duration

Weld bead geometry was quantified using an Optive Lite OLM 3020 vision measuring system equipped with VMS 3.1 software. Bead width was measured at selected locations along the weld, and the average value was used for subsequent analysis. For metallographic examination, the welded coupons were sectioned across the joint using wire electrical discharge machining (WEDM). The specimens were then mounted, ground using progressively finer silicon carbide (SiC) abrasive papers, and polished with diamond suspension to obtain a mirror-like surface finish. Final polishing was performed using HiFin polishing lubricant. The polished surfaces were etched for approximately 3 s using a solution of HNO_3-HF-CH_3COOH mixed in a 2:2:2 volume ratio to reveal the weld microstructure. Microstructural examination and fracture surface characterization were performed using a Thermo Scientific Apreo S field-emission scanning electron microscope (FESEM). Energy-dispersive X-ray spectroscopy (EDS), coupled with the FESEM, was used to analyse the elemental composition of the fusion zone and assess elemental redistribution during welding.

Crystallographic orientation, grain morphology, grain size, and grain boundary characteristics were characterized using electron backscatter diffraction (EBSD) on an FEI Quanta 3D scanning electron microscope fitted with an EBSD detector. Prior to EBSD acquisition, the specimens were mechanically polished and electro-polished to eliminate surface deformation. Data were collected at an accelerating voltage of 20 kV with a 1 μm scanning step size and processed using OIM-TSL software. Phase identification was performed using a Bruker D8 Advance DaVinci X-ray diffractometer equipped with Cu Kα radiation. The instrument was operated at 40 kV and 45 mA, and diffraction patterns were recorded over a 2θ range of 10°-100° to identify the crystalline phases present in the base material and welded region.

The hardness distribution across the welded joint was evaluated using a Kelly HDNX micro-Vickers hardness tester in accordance with ASTM E384. Measurements were performed under a load of 500 gf with a dwell time of 10 s. Indentations were made across the weld cross-section, covering the fusion zone, fusion boundary, heat-affected zone (HAZ), and base material, to characterize the spatial variation in hardness. Mechanical performance was assessed by uniaxial tensile testing using an Instron 6800 universal testing machine controlled through Bluehill Universal software. Tensile specimens were prepared in accordance with ASTM F2516 and tested at ambient conditions (32 °C and approximately 80% relative humidity) using a crosshead speed of 0.5 mm min^{-1}. Three specimens were tested for each welding condition, and the average values were used for analysis.

The phase transformation behavior of the base material and welded joints was investigated using a NETZSCH DSC 214 Polyma differential scanning calorimeter. Measurements were conducted over a temperature range of -40 °C to 100 °C under a controlled heating/cooling program using aluminium crucibles to determine the characteristic transformation temperatures. Electrochemical corrosion performance was evaluated through potentiodynamic polarization (PDP) testing using an IVIUM electrochemical workstation in 0.9 wt.% NaCl solution in accordance with ASTM G61-86. The welded specimen served as the working electrode, graphite as the counter electrode, and a saturated calomel electrode (SCE) as the reference electrode. Polarization scans were performed between −1.0 V and +1.0 V (vs. SCE). The corrosion potential, corrosion current density, open-circuit potential, and corrosion rate were subsequently determined using the IVIUM electrochemical analysis software.

3. Results and discussion

3.1 Macrostructure of Pulse Duration Samples in DP-TIG Welding

Complete joint penetration was achieved for all three pulse duration conditions, indicating that the selected welding parameters were sufficient to produce sound autogenous welds in the 1 mm thick Nitinol sheets. The macrographs of the welded joints corresponding to pulse duration ratios of 50–50%, 40–60%, and 60–40% are shown in **Fig. 2(a–c)**, while the measured bead geometry is summarized in **Table 2.** All welded specimens exhibited a nearly rectangular weld bead profile with a uniform depth of penetration of 1 mm, confirming complete penetration through the sheet thickness. Although the depth of penetration remained unchanged, the bead width varied with pulse duration. Among the investigated conditions, the 40–60% pulse duration produced the narrowest weld bead (3.64 mm), whereas the 50–50% and 60–40% pulse duration conditions resulted in bead widths of 3.70 mm and 3.82 mm, respectively. Compared with the 40–60% condition, the bead width increased by 1.64% for the 50–50% pulse duration and by 4.94% for the 60–40% pulse duration.

The reduction in bead width observed at the 40–60% pulse duration can be attributed to the shorter peak current duration and the relatively longer base current period, which promoted a lower effective heat input and restricted lateral heat diffusion within the weld pool. Consequently, the molten metal experienced a higher cooling rate, resulting in a narrower fusion zone while maintaining complete penetration. In contrast, the longer peak current duration employed in the 60–40% pulse duration increased the thermal energy delivered to the joint, allowing greater spreading of the molten pool and producing a wider weld bead. These observations demonstrate that pulse duration is an effective parameter for controlling weld bead geometry by regulating the thermal cycle and molten pool behavior during the DPTIG welding process.

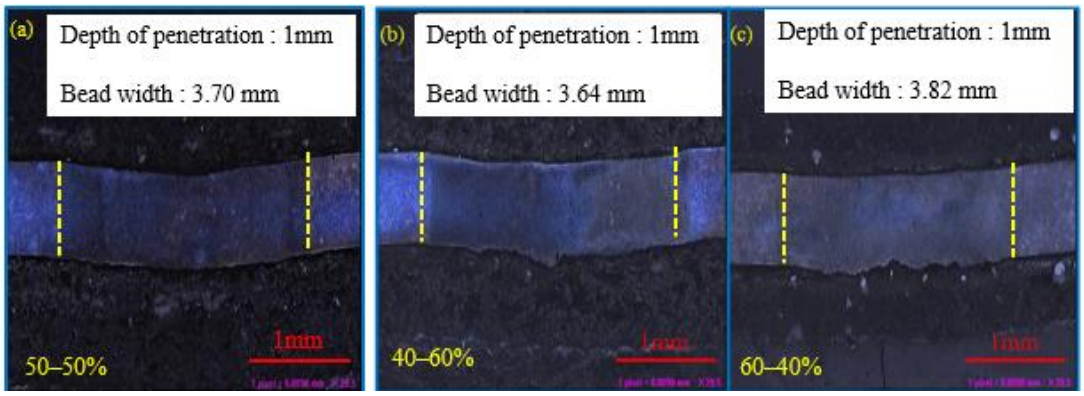


Figure 2. Macrostructure of DPTIG welded samples (a) 50-50 %, (b) 40-60% and (c) 60-40 %

Table 2. Bead geometry of pulse duration samples

Sl.No.	Pulse duration	Bead width (mm)	Depth of penetration (mm)
1	(50–50)%	3.70	1
2	(40–60)%	3.64	1
3	(60–40)%	3.82	1

3.2 Characterization of the welded joint

3.2.1 Microstructure of Pulse Duration Samples in DPTIG Welding

The fusion zone (FZ) microstructures corresponding to pulse duration ratios of 50–50%, 40–60%, and 60–40% are presented in **Fig. 3(a–c)**. Irrespective of the pulse duration, all welded joints exhibited a predominantly columnar grain morphology, which is characteristic of fusion-welded NiTi alloys. The grains nucleated epitaxially from the fusion boundary and propagated towards the weld centreline along the direction of the maximum thermal gradient during solidification. No solidification cracks or porosity were observed in any of the welded joints, confirming the effectiveness of the DPTIG process in producing defect-free welds. The base metal and fusion zone predominantly consisted of the B2 austenite phase. However, the grain morphology was significantly influenced by pulse duration. The 40–60% pulse duration condition produced the finest columnar grains. In comparison, the 50–50% and 60–40% pulse duration conditions resulted in comparatively coarser columnar grains. The reduction in grain size at the 40–60% pulse duration is attributed to the lower thermal energy supplied to the weld pool, which increased the cooling rate and reduced the solidification time. The rapid heat extraction restricted the growth of columnar dendrites and promoted grain refinement. Conversely, the higher heat inputs associated with the 50–50% and particularly the 60–40% pulse durations prolonged the molten pool lifetime, reduced the cooling rate, and facilitated grain coarsening. Similar grain refinement under reduced heat input has been reported for fusion-welded NiTi alloys, where rapid solidification suppresses grain growth and improves the weld microstructure. The refined columnar grains obtained under the 40–60% pulse duration are expected to enhance the mechanical performance through grain-boundary strengthening (Hall-Petch relationship), which is further confirmed by the higher hardness and tensile strength presented in the subsequent sections.

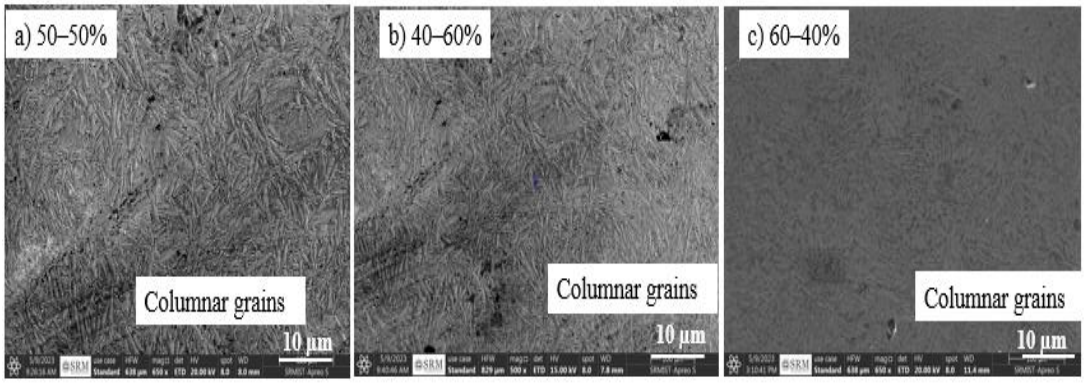


Figure 3 Microstructure of (a) pulse duration 50–50%, (b) pulse duration 40–60%, and (c) pulse duration 60-40%

3.2.2 Phase Mapping of Pulse Duration Samples in DPTIG Welding

The EBSD phase maps of the welded joints produced at pulse duration ratios of 50–50%, 40–60%, and 60–40% are presented in **Fig. 4(a–c).** Irrespective of the pulse duration, the fusion zone was predominantly composed of the B2 austenite phase, with only a negligible fraction of martensite. The predominance of the austenitic phase indicates that the selected DPTIG welding parameters did not significantly alter the phase constitution of the Nitinol alloy and that the fusion zone retained the high-temperature B2 structure after solidification. Although all three welding conditions exhibited a similar phase distribution, slight variations in the martensite fraction were observed, which may be associated with differences in the thermal cycle and cooling rate resulting from the variation in pulse duration. The relatively lower heat input associated with the 40–60% pulse duration promoted rapid cooling, thereby stabilizing the austenitic matrix while suppressing the formation of martensite. Consequently, the welded joint retained a predominantly B2 austenitic microstructure with refined grains.

In addition to the B2 austenite phase, X-ray diffraction confirmed the presence of secondary phases, including TiO_2, Ti_2Ni, and Ni_3Ti, in the fusion zone. The formation of Ti_2Ni and Ni_3Ti is attributed to elemental segregation and non-equilibrium solidification during fusion welding, whereas the presence of TiO_2 results from the oxidation of titanium during the welding process despite argon shielding. These intermetallic compounds are known to influence the mechanical performance and corrosion behaviour of welded Nitinol joints by increasing local brittleness and modifying the electrochemical characteristics of the fusion zone. However, their formation was limited under the optimized DPTIG welding conditions because of the comparatively lower heat input and improved molten pool dynamics. The predominance of the B2 austenite phase together with the limited formation of secondary intermetallic phases demonstrates that the DPTIG process effectively preserves the phase stability of Nitinol while providing favourable solidification conditions. This phase stability is expected to contribute to the improved tensile properties and controlled phase transformation behaviour discussed in the subsequent sections.

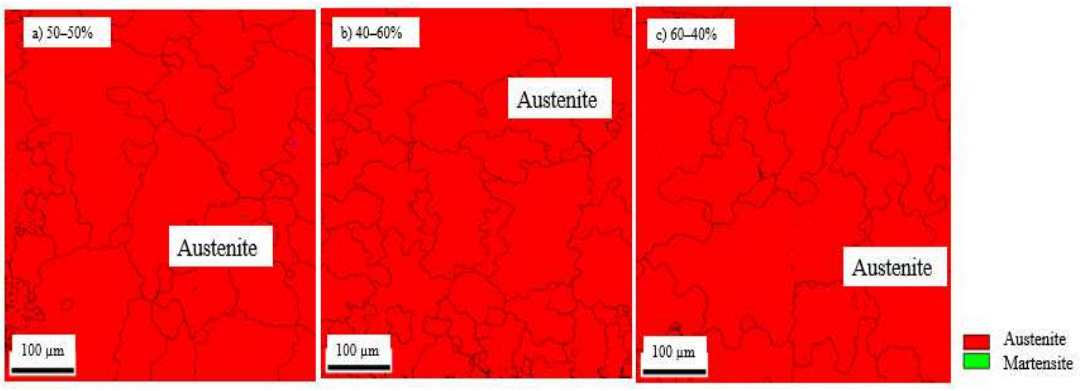


Figure 4 Phase fraction of (a) pulse duration 50–50%, (b) pulse duration 40–60%, and (c) pulse duration 60 -40%

3.2.3 Average Grain Size of Pulse Duration Samples

The inverse pole figure (IPF) maps of the fusion zone obtained at pulse-duration ratios of 50–50%, 40–60%, and 60–40% are presented in **Fig. 5(a–c),** respectively. The average grain size was determined using the linear intercept method, yielding values of 26 ± 3 µm, 24 ± 2 µm, and 30 ± 3 µm for the respective conditions. Among the investigated conditions, the 40–60% ratio produced the finest grain structure. This refinement may be attributed to a reduction in effective heat input and a higher cooling rate, which shorten the solidification time and restrict grain growth. Conversely, the 60–40% ratio resulted in the coarsest grains, potentially owing to the greater thermal energy input associated with the longer peak-current duration, which promotes grain growth. The finer grain structure obtained at the 40–60% ratio may contribute to improved mechanical strength through the Hall-Petch mechanism, whereby increased grain boundary density impedes dislocation motion.

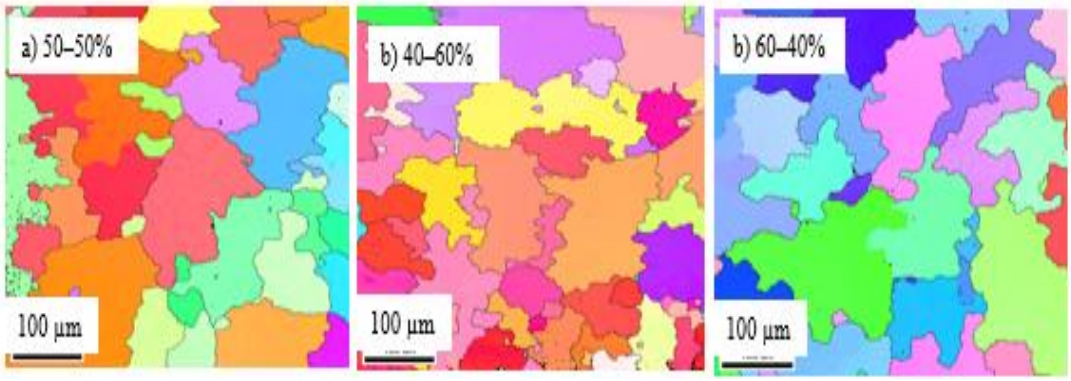


Figure 5 Inverse pole figure of (a) pulse duration 50-50%, b) pulse duration 40-60%, and (c) pulse duration 60-40%

3.2.4 Grain Boundary Angle of Pulse Duration Samples

The grain boundary misorientation maps of the fusion zone corresponding to pulse duration ratios of 50–50%, 40–60%, and 60–40% are presented in **Fig. 6(a–c).** The grain boundaries were classified as low-angle grain boundaries (LAGBs, 2°–15°) and high-angle grain boundaries (HAGBs, >15°) to evaluate the influence of pulse duration on the grain boundary characteristics of the welded joints. The 50–50%, 40–60%, and 60–40% pulse duration conditions exhibited HAGB fractions of 75%, 76%, and 72%, respectively, whereas the corresponding LAGB fractions were 25%, 24%, and 28%. Among the investigated conditions, the 40–60% pulse duration exhibited the highest HAGB fraction and the lowest LAGB fraction. This behaviour is attributed to the lower effective heat input, which promoted rapid solidification and grain refinement during weld metal solidification. The finer grain structure observed under the 40–60% pulse duration increased the proportion of high-angle grain boundaries, indicating a more refined and stable microstructure. High-angle grain boundaries act as effective barriers to dislocation motion and contribute to grain boundary strengthening. Consequently, the increased HAGB fraction in the 40–60% pulse duration is expected to enhance the mechanical performance of the welded joint, which is consistent with the higher tensile strength observed in the subsequent mechanical characterization. Conversely, the 60–40% pulse duration, which exhibited the lowest HAGB fraction and coarser grains, is expected to offer comparatively lower resistance to plastic deformation.

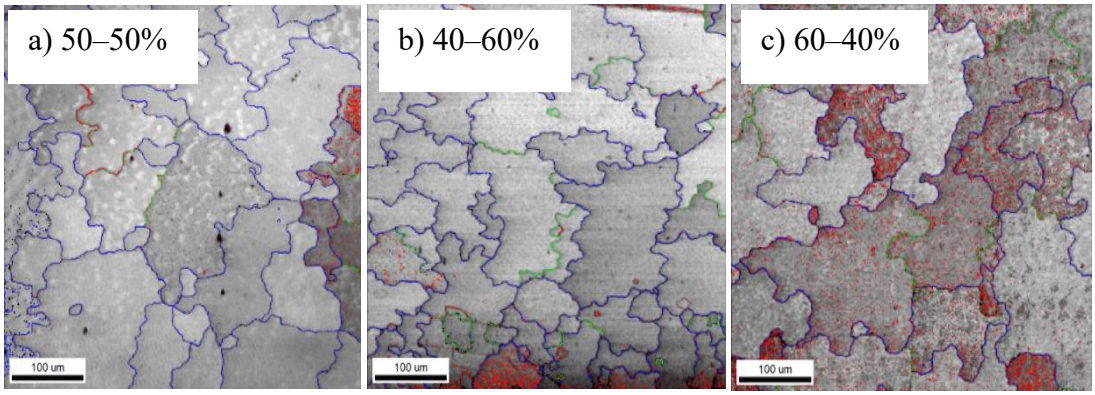


Figure 6 Grain boundary maps of (a) pulse duration (50–50%) (b) pulse duration (40–60%), and (c) pulse duration (60-40%)

3.2.6 Kernel Average Misorientation of Pulse Duration Samples

The kernel average misorientation (KAM) maps of the fusion zone obtained at pulse-duration ratios of 50–50%, 40–60%, and 60–40% are presented in Fig. 7(a–c), respectively. KAM analysis was used to assess local crystallographic misorientation and lattice distortion within the welded microstructure. Higher KAM values generally indicate greater local lattice curvature and may be associated with increased geometrically necessary dislocation (GND) density, whereas lower values suggest reduced local misorientation. The average KAM values for the 50–50%, 40–60%, and 60–40% conditions were 4.92°, 4.87°, and 4.98°, respectively. The 40–60% condition exhibited the lowest average KAM value, suggesting comparatively lower local lattice distortion and GND density in the fusion zone. This behaviour may be associated with differences in the thermal history and solidification conditions resulting from pulse-duration modulation. In contrast, the slightly higher KAM values for the 50–50% and 60–40% conditions indicate greater local crystallographic misorientation. The lower KAM value observed for the 40–60% condition, together with its finer grain structure and higher fraction of high-angle grain boundaries, provides complementary evidence of differences in the weld microstructure and is consistent with the superior tensile strength observed under this condition.

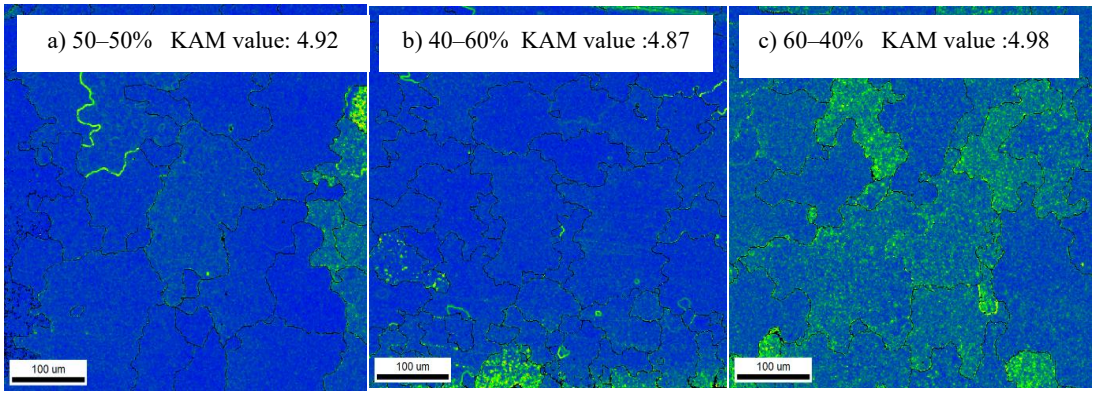


Figure 7 KAM maps of a) pulse duration 50–50% b) pulse duration 40–60%, c) pulse duration 60-40%

3.2.7 Pole Figures of Pulse Duration Samples

The crystallographic texture of the fusion zone corresponding to pulse duration ratios of 50–50%, 40–60%, and 60–40% is presented in the pole figures shown in **Fig. 8(a–c).** The texture was analysed along the {001}, {111}, and {110} crystallographic planes to evaluate the influence of pulse duration on grain orientation during solidification. All the welded samples exhibited a moderate texture, with the {001} and {111} orientations showing higher pole densities than the {110} orientation. The maximum pole intensities for the 50–50%, 40–

60%, and 60–40% pulse duration conditions were 16.20, 20.20, and 11.43, respectively. Among the investigated conditions, the 40–60% pulse duration exhibited the highest texture intensity, indicating a relatively stronger preferred crystallographic orientation in the fusion zone. The enhanced texture intensity observed under the 40–60% pulse duration is attributed to the lower effective heat input and the corresponding increase in cooling rate, which influenced grain growth during solidification and promoted a more uniform crystallographic orientation. In contrast, the relatively lower pole intensity observed for the 60–40% pulse duration may be associated with increased heat input, resulting in grain coarsening and a less uniform solidification structure. Variations in solidification behaviour, grain morphology, and the precipitation of secondary phases can also influence the development of crystallographic texture during welding. The stronger texture developed under the 40–60% pulse duration, together with the finer grain structure and higher fraction of high-angle grain boundaries, contributed to the improved mechanical performance of the welded joints. The crystallographic texture of the fusion zone corresponding to pulse duration ratios of 50–50%, 40–60%, and 60–40% is presented in the pole figures shown in **Fig. 8(a–c).** The texture was analysed along the {001}, {111}, and {110} crystallographic planes to evaluate the influence of pulse duration on grain orientation during solidification. All the welded samples exhibited a moderate texture, with the {001} and {111} orientations showing higher pole densities than the {110} orientation. The maximum pole intensities for the 50–50%, 40–60%, and 60–40% pulse duration conditions were 16.20, 20.20, and 11.43, respectively. Among the investigated conditions, the 40–60% pulse duration exhibited the highest texture intensity, indicating a relatively stronger preferred crystallographic orientation in the fusion zone. The enhanced texture intensity observed under the 40–60% pulse duration is attributed to the lower effective heat input and the corresponding increase in cooling rate, which influenced grain growth during solidification and promoted a more uniform crystallographic orientation. In contrast, the relatively lower pole intensity observed for the 60–40% pulse duration may be associated with increased heat input, resulting in grain coarsening and a less uniform solidification structure. Variations in solidification behaviour, grain morphology, and the precipitation of secondary phases can also influence the development of crystallographic texture during welding. The stronger texture developed under the 40–60% pulse duration, together with the finer grain structure and higher fraction of high-angle grain boundaries, contributed to the improved mechanical performance of the welded joints.

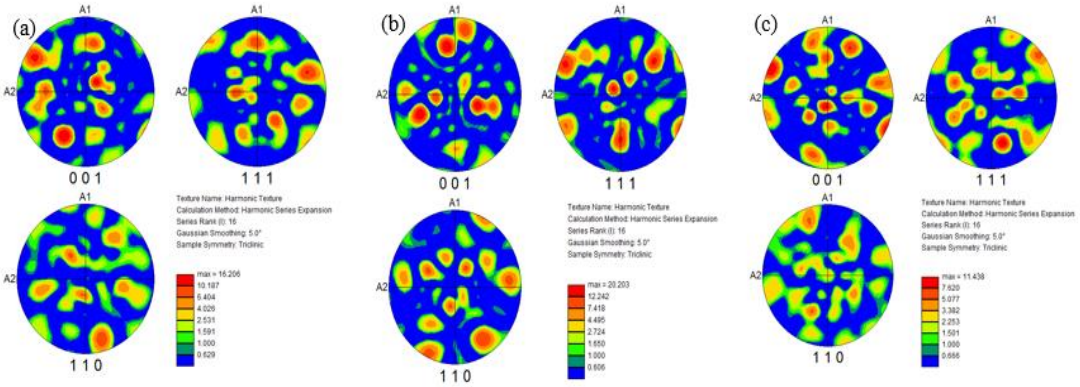


Figure 8 Pole figures of a) pulse duration 50–50% b) pulse duration 40–60% c) pulse duration 60-40%

3.2.8 X-Ray Diffraction Analysis of Pulse Duration Samples

The X-ray diffraction (XRD) patterns of the base material and DPTIG-welded Nitinol joints corresponding to pulse duration ratios of 50–50%, 40–60%, and 60–40% are presented in **Fig. 9**. The base material predominantly exhibited diffraction peaks corresponding to the B2 austenite phase, together with a small fraction of the B19′ martensite phase, indicating the dual-phase nature of the as-received Nitinol alloy. The welded samples also retained the B2 austenite phase; however, additional diffraction peaks corresponding to Ti_2Ni and Ni_3Ti intermetallic phases were observed in the fusion zone. The formation of Ti_2Ni and Ni_3Ti is attributed to the rapid melting and solidification experienced during the DPTIG welding process, which promotes elemental redistribution and local compositional variations within the weld pool. Such non-equilibrium solidification conditions favour the precipitation of secondary intermetallic compounds in the fusion zone. Although these phases were detected under all pulse duration conditions, their formation is expected to depend on the welding thermal cycle and the associated heat input. The comparatively lower heat input associated with the 40–60% pulse duration is expected to suppress excessive intermetallic precipitation by reducing the residence time of the molten pool at elevated temperatures. The precipitation of Ti_2Ni and Ni_3Ti has been widely reported in fusion-welded

NiTi alloys and is known to influence the mechanical and electrochemical performance of welded joints. These intermetallic phases act as brittle constituents that can reduce ductility and tensile strength while also affecting the passive behaviour of the alloy in corrosive environments. Therefore, controlling the welding thermal cycle through pulse duration modulation is essential for minimizing intermetallic phase formation and preserving the structural and functional characteristics of DPTIG-welded Nitinol joints.

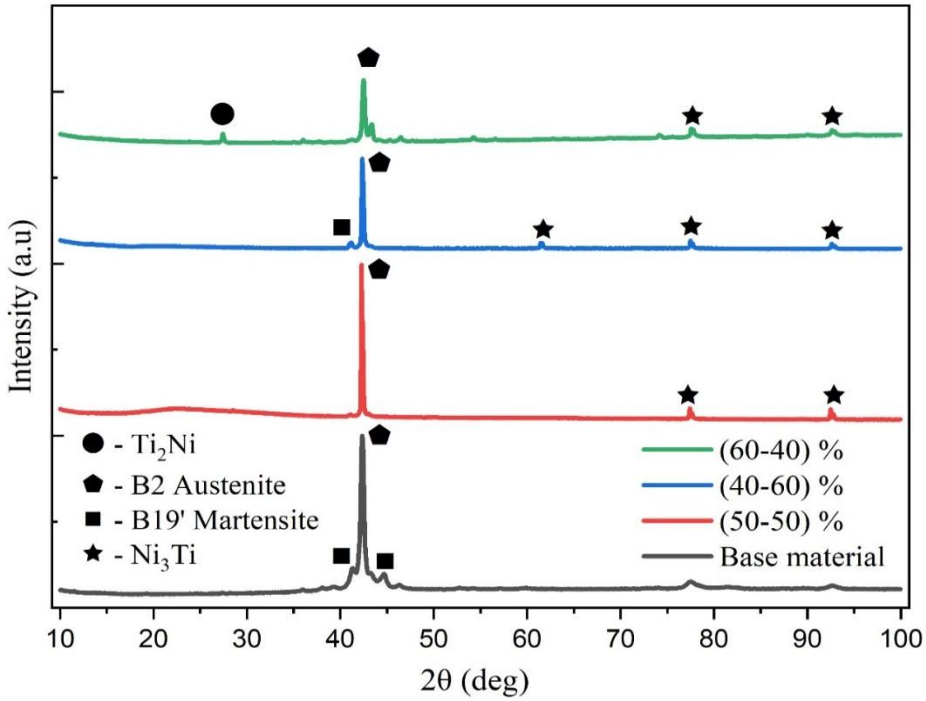


Figure 9 XRD graph of the BM, pulse duration 50–50%, pulse duration 40–60%, pulse duration 60 – 40%

3.3 Micro-hardness of Pulse Duration Samples

The microhardness values measured across the fusion zone (FZ) and heat-affected zone (HAZ) of the DPTIG-welded joints are summarized in **Table 3**. Three indentations were made in each region, and the average value was considered for analysis. The base material exhibited an average hardness of 370 ± 8 HV. The fusion zone hardness for the 50–50%, 40–60%, and 60–40% pulse duration conditions was 284 ± 12 HV, 292 ± 14 HV, and 268 ± 12 HV, respectively. Among the investigated conditions, the 40–60% pulse duration exhibited the highest fusion zone hardness, whereas the 60–40% pulse duration showed the lowest value. The relatively higher hardness obtained at the 40–60% pulse duration is attributed to the lower effective heat input, which promoted a higher cooling rate and resulted in finer columnar grains. According to the Hall–Petch relationship, grain refinement increases the resistance to dislocation motion, thereby improving hardness. In contrast, the higher thermal energy associated with the 60–40% pulse duration promoted grain coarsening during solidification, leading to a reduction in fusion zone hardness. The HAZ exhibited hardness values of 372 ± 4 HV, 376 ± 6 HV, and 370 ± 6 HV for the 50–50%, 40–60%, and 60–40% pulse duration conditions, respectively, which were comparable to or slightly higher than those of the base material. This behaviour is attributed to the limited microstructural modification within the HAZ, where the material retained a relatively fine microstructure and experienced less severe melting than the fusion zone. Overall, the fusion zone exhibited lower hardness than the base material owing to grain coarsening and microstructural changes associated with fusion welding. Although Ti_2Ni and Ni_3Ti intermetallic phases were detected by XRD, the overall hardness of the fusion zone was predominantly governed by grain size and the weld thermal cycle.

Table 3 Micro-hardness in FZ and HAZ of pulse duration samples

Pulse duration	FZ (HV)	HAZ (HV)
(50–50)%	284 ± 12	372 ± 4
(40–60)%	292 ± 14	376 ± 6

(60–40)%	268 ± 12	370 ± 6

3.4 Tensile Test of Pulse Duration Samples

The engineering stress-strain curves of the DPTIG-welded Nitinol joints produced under different pulse duration conditions are presented in **Fig. 10**, and the corresponding ultimate tensile strength (UTS) values are summarized in **Table 4.** The base material exhibited a UTS of 700 ± 12 MPa with an elongation of 11.6 ± 0.3%. The welded joints produced under pulse duration ratios of 50–50%, 40–60%, and 60–40% exhibited UTS values of 566 ± 8 MPa, 583 ± 11 MPa, and 529 ± 9 MPa, respectively.Compared with the base material, all welded joints exhibited lower tensile strength owing to the microstructural changes induced by the fusion welding process, including grain growth, thermal softening, local compositional variations, and the formation of Ti_2Ni and Ni_3Ti intermetallic phases. Among the investigated conditions, the 40–60% pulse duration exhibited the highest tensile strength (583 ± 11 MPa), representing an improvement of approximately 3% over the 50–50% pulse duration. This superior mechanical performance is attributed to the relatively lower effective heat input, which promoted rapid solidification and resulted in finer columnar grains (24 ± 2 μm), the highest HAGB fraction (76%), the lowest KAM value (4.87°), and the highest fusion zone hardness (292 ± 14 HV). Collectively, these microstructural characteristics enhanced resistance to dislocation motion and improved the load-bearing capacity of the welded joint. In contrast, the 60–40% pulse duration exhibited the lowest tensile strength (529 ± 9 MPa). The longer peak-current duration increased the thermal energy supplied to the weld pool, resulting in grain coarsening (30 ± 3 μm), a lower HAGB fraction (72%), and reduced fusion zone hardness (268 ± 12 HV), which collectively diminished the strength of the welded joint.

The welded joints exhibited elongation values of 13.27 ± 0.4%, 15.53 ± 0.2%, and 17.33 ± 0.3% for the 50–50%, 40–60%, and 60–40% pulse duration conditions, respectively. The increase in elongation with increasing pulse duration indicates a trade-off between strength and ductility. The higher heat input associated with the 60–40% pulse duration promoted grain coarsening and reduced the resistance to plastic deformation, resulting in lower tensile strength but greater ductility. These results demonstrate that optimizing the pulse duration enables a favourable balance between mechanical strength and ductility in autogenous DPTIG-welded Nitinol sheets.

Table 4 Effect of pulse duration on tensile strength

Pulse duration (Peak current- base current)	Tensile strength (MPa)
50-50%	566 ± 8
40-60%	583 ± 11
60-40%	529 ± 9

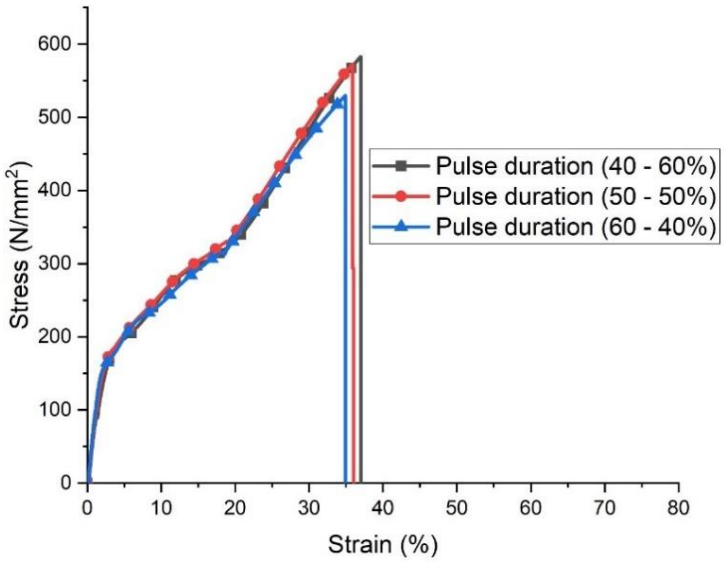


Figure 10 Stress-strain graph of pulse duration samples

The fracture surfaces of the tensile-tested DPTIG-welded Nitinol joints corresponding to pulse duration ratios of 50–50%, 40–60%, and 60–40% are presented in **Fig. 11(a-c).** Irrespective of the pulse duration, the fractured surfaces exhibited a combination of dimples and cleavage facets, indicating a mixed ductile–brittle fracture mode.Among the investigated conditions, the 40–60% pulse duration exhibited a relatively higher density of fine and uniformly distributed dimples, suggesting greater plastic deformation prior to fracture. This behaviour is consistent with the finer grain structure, higher HAGB fraction, lower KAM value, and higher fusion zone hardness observed in the EBSD and microhardness analyses, which collectively contributed to the highest tensile strength (583 ± 11 MPa). In contrast, the 60–40% pulse duration exhibited comparatively larger cleavage facets with fewer dimples, indicating an increased contribution of brittle fracture. The higher heat input associated with this pulse duration promoted grain coarsening and facilitated the formation of brittle intermetallic phases, resulting in the lowest tensile strength (529 ± 9 MPa).The coexistence of dimples and cleavage facets demonstrates that fracture of the DPTIG-welded Nitinol joints occurred through a mixed fracture mechanism. The variation in the relative proportion of ductile and brittle features with pulse duration confirms that the welding thermal cycle significantly influences the fracture behaviour and mechanical performance of the welded joints.

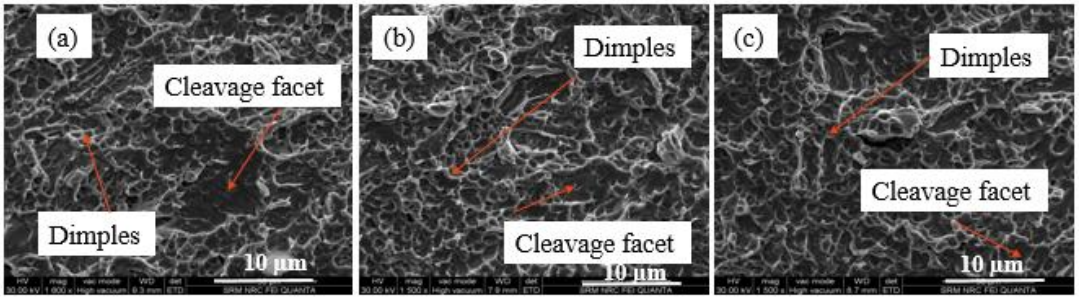


Figure 11 Fractography of (a) pulse duration 50–50% (b) pulse duration 40–60% (c) pulse duration 60-40%

3.5 Phase Transformation Temperature of Pulse Duration Samples

The DSC thermograms of the base material and DPTIG-welded Nitinol joints corresponding to pulse duration ratios of 50–50%, 40–60%, and 60–40% are presented in **Fig. 12(a–d).** During cooling, the alloy transformed from the B2 austenite phase to the B19′ martensite phase, whereas the reverse transformation from B19′ martensite to B2 austenite occurred during heating. No intermediate R-phase transformation was observed in either the base material or the welded samples, indicating that the selected welding conditions did not promote a two-stage phase transformation. The phase transformation temperatures and thermal hysteresis were influenced by the welding thermal cycle. Compared with the base material, all welded joints exhibited variations in transformation behaviour due to the thermal effects associated with fusion welding. Among the investigated conditions, the 40–60% pulse duration exhibited the smallest deviation in thermal hysteresis, indicating that this welding condition better preserved the functional characteristics of the Nitinol alloy. The relatively lower effective heat input promoted rapid cooling and minimized microstructural alterations, thereby reducing the changes in transformation behaviour. The observed variations in thermal hysteresis among the welded joints are attributed to the combined effects of the welding thermal cycle, including local compositional redistribution, residual lattice strain, and the formation of Ti_2Ni and Ni_3Ti intermetallic phases. These microstructural changes influence the stability of the B2 and B19′ phases and consequently modify the martensitic transformation behaviour. The smaller hysteresis observed for the 40–60% pulse duration suggests improved phase stability, making this welding condition more suitable for applications requiring reliable shape memory and superelastic performance.

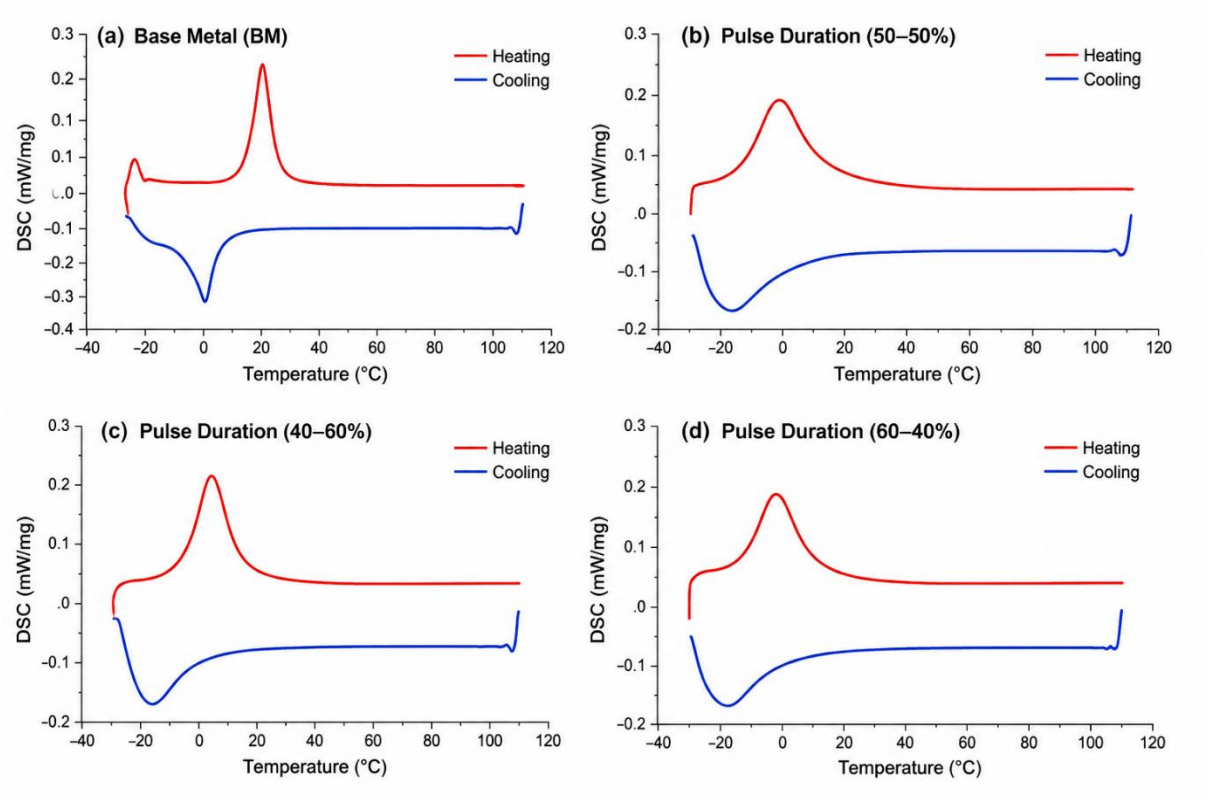


Figure 12 Differential scanning calorimeter graphs of (a) base metal, (b) pulse duration 50–50% pulse duration 40–60% (d) pulse duration 60-40%

3.6 Corrosion Test of Pulse Duration Samples

The corrosion behaviour of the DPTIG-welded Nitinol joints was evaluated using potentiodynamic polarization (PDP), and the corresponding polarization curves are presented in **Fig. 13(a–c).** The electrochemical parameters, including the corrosion potential (Ecorr) and corrosion rate, are summarized in **Table 4.** The measured Ecorr values for the 50–50%, 40–60%, and 60–40% pulse duration conditions were −0.0873 V, −0.1972 V, and −0.2055 V, respectively. The corresponding corrosion rates were 0.005657 mm/year, 0.00443 mm/year, and 0.00402 mm/year, indicating that the 60–40% pulse duration exhibited the lowest corrosion rate among the investigated conditions. Furthermore, all welded joints showed lower corrosion rates than the base material, demonstrating that the DPTIG welding process did not adversely affect the corrosion performance of the Nitinol sheets.

The superior corrosion resistance observed for the 60–40% pulse duration is attributed to the formation of a stable passive TiO_2 film on the weld surface, which effectively limited metal dissolution in the physiological saline solution. In addition, the welding thermal cycle influenced the distribution of secondary phases and the microstructural homogeneity of the fusion zone, thereby affecting the electrochemical behaviour of the welded joints. Although Ti_2Ni and Ni_3Ti intermetallic phases were identified in the fusion zone, the lower corrosion rate obtained for the 60–40% pulse duration suggests that the passive oxide film provided effective protection against localized corrosion under the present welding conditions. Overall, the PDP results demonstrate that pulse duration significantly influences the corrosion behaviour of DPTIG-welded Nitinol. While the 40–60% pulse duration produced superior mechanical properties through grain refinement, the 60–40% pulse duration exhibited the best corrosion performance, highlighting the trade-off between mechanical strength and corrosion resistance.

Table 4 Results of the corrosion tests for the pulse duration samples

Pulse duration	E_{corr} (V)	Corrosion rate (mm/year)
(50–50) %	–0.0873	0.005657
(40–60) %	–0.1972	0.00443
(60–40) %	–0.2055	0.00402

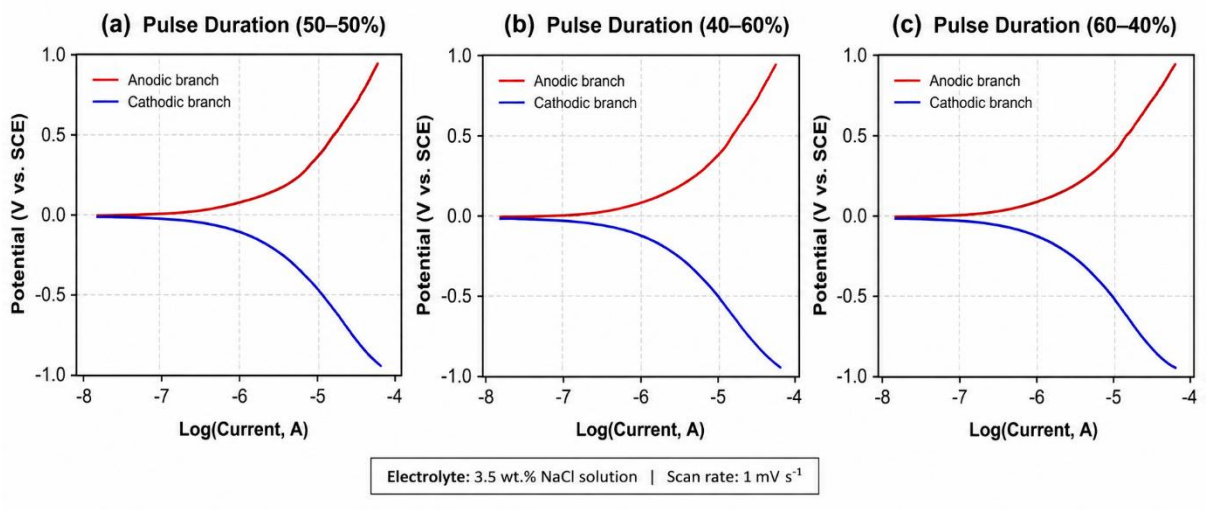


Figure 13 Tafel curves of the (a) pulse duration 50–50%, (b) pulse duration 40–60%, and (c) pulse duration 60 – 40%

4. Conclusions

- Autogenous double-pulse tungsten inert gas (DPTIG) welding was successfully employed to join 1 mm-thick Nitinol sheets using pulse-duration ratios of 50–50%, 40–60%, and 60–40%. The effects of pulse-duration ratio on weld bead geometry, microstructure, mechanical properties, phase transformation behaviour, and corrosion resistance were systematically investigated. The major findings are summarized as follows:
- Full-penetration welds were achieved under all pulse-duration conditions. The 40–60% condition produced the narrowest bead width (3.64 mm), indicating improved control over weld geometry.
- The fusion zone predominantly comprised B2 austenite with a columnar grain morphology. XRD analysis identified Ti_2Ni and Ni_3Ti intermetallic phases in all welded joints. The 40–60% condition yielded the finest grain size (24 ± 2 μm), the highest high-angle grain boundary (HAGB) fraction (76%), and the lowest average kernel average misorientation (KAM) value (4.87°), indicating a refined microstructure with comparatively lower local crystallographic misorientation.
- The 40–60% condition exhibited the highest fusion-zone hardness (292 ± 14 HV) and ultimate tensile strength (583 ± 11 MPa), representing an approximately 3% increase in tensile strength compared with the 50–50% condition. This improvement is consistent with the combined effects of grain refinement and increased HAGB fraction, although the individual contributions of these factors require further confirmation.
- Differential scanning calorimetry (DSC) revealed the B2 ↔ B19′ transformation, with no discernible R-phase transformation peak. Among the investigated conditions, the 40–60% condition exhibited the smallest deviation in phase transformation behaviour, suggesting better preservation of the transformation characteristics of Nitinol following welding.
- Potentiodynamic polarization tests showed that the 60–40% condition exhibited the lowest corrosion rate (0.00402 mm/year), indicating the best corrosion performance among the investigated conditions. This behaviour may be associated with differences in the electrochemical characteristics and passive-film stability of the welded microstructure.
- Overall, pulse-duration ratio significantly influenced weld geometry, microstructural evolution, mechanical performance, phase transformation behaviour, and corrosion resistance during DPTIG welding of thin Nitinol sheets. The 40–60% condition provided the most favourable combination of weld geometry, grain refinement, mechanical properties, and phase transformation behaviour, whereas the 60–40% condition exhibited the lowest corrosion rate. These findings highlight the potential of DPTIG welding as an alternative joining technique for thin Nitinol components in biomedical and precision-engineering applications.

Funding The author(s) received no financial support for the research, authorship, and/or publication of this article.

Data availability The authors confirm that the data supporting the findings of this study are available within the article.

Code availability Not applicable.

Declarations

Conflict of interest The author(s) declared no potential conflicts of interest with respect to the research, authorship, and/or publication of this article.

Ethics approval Not applicable

Athor Contribution: Manoj Samson R: Methodology, Investigation, Project administration, Writing-original draft, Validation, Formal analysis; **R Saravanakumar**: Investigation, Writing-original draft, Validation, Formal analysis; **Sanjeev Kumar**: Writing-original draft, Formal analysis, **Chandan Pandey**: Investigation, Writing-original draft, Validation, Formal analysis, Methodology

References:

[1] Gholizadeh, S. and Sivarasu, S. (2026) 'Nitinol shape memory alloy (NiTi SMA): Materials and applications in medical devices', *Journal of Applied Biomaterials & Functional Materials*, 24, pp. 1–29.
[2] Bouchareb, N., Fellah, M., Hezil, N., Guesmi, A. and Khezami, L. (2026) 'A review of Nitinol shape memory alloys for biomedical applications: Advancements and biocompatibility', *JOM*, 78(1), pp. 140–167.
[3] 'Essential concerns of NiTi shape memory alloys and their advancement in additive manufacturing' (2025) *Materials Today Communications*, 48, 113546.

[4] Yan, K., Chu, K., Wang, M., Hua, P., Wei, P., Gu, H., Zhuang, Q., He, W., Sun, Q., Ritchie, R.O. and Ren, F. (2026) 'Bending-fatigue-resistant hierarchical NiTi shape memory alloy', *Nature Communications*, 17, 6376.

[5] Dong, P., Yao, R., Yan, Z., Yan, Z., Wang, W., He, X. and Zhou, J. (2018). Microstructure and corrosion resistance of laser-welded crossed Nitinol wires. Materials, 11(5), 842.
[6] Datta, S., Chakraborty, R., Raza, M.S., Saha, P. and Pratihar, D.K. (2023). "Comparative study on weld characterisation and corrosion performance of laser-welded NiTinol." Science and Technology of Welding and Joining, 28(8).
[7] Zailani, Z.A., Rosli, M.H., Noor, N.Z.M. and Mativenga, P., 2026. Machining-induced machinability and phase transformation behaviour of nickel–titanium shape memory alloys under graphene NanoMQL and chilled air assisted milling. The International Journal of Advanced Manufacturing Technology, pp.1-15.
[8] Bertolini, R., Tucci, F., Ghiotti, A., Jawahir, I.S. and Bruschi, S., 2025. Analysis of tool wear and surface integrity in turning wrought and additively manufactured Ni50. 8Ti49. 2 shape memory alloys. Wear, 570, p.205890.
[9] Mwangi, J. W., Nguyen, L. T., Bui, V. D., Berger, T., Zeidler, H., and Schubert, A. (2019). "Nitinol manufacturing and micromachining: A review of processes and their suitability in processing medical-grade nitinol." Journal of Manufacturing Processes, 38, 355–369.
[10] Mehrpouya, M., Gisario, A., and Elahinia, M. (2018). "Laser welding of NiTi shape memory alloy: A review." Journal of Manufacturing Processes, 31, 162–186.
[11] Zhang, K., Li, J., Anousheh, A., Li, J., Parniani, F., Zang, C., Tang, X.S. and Peng, P., 2025. Interfacial liquid control to realize superior comprehensive properties of microwelded NiTi-stainless steel joints for multifunctional biomedical device fabrication. Journal of Materials Science & Technology, 233, pp.304-318.
[12] Q.M. Yaseen, R.M. Gul, M.N. Baig, F.N. Khan, M.A. Kamran, M.K.U. Khalil, *Laser beam welding of NiTi shape memory alloy sheets: Microstructural evolution and mechanical properties*, Next Materials, 11 (2026), 101695.
[13] Otsuka, K. and Ren, X. (2005). "Physical metallurgy of Ti–Ni-based shape memory alloys." Progress in Materials Science, 50(5), 511–678.
[14] Kannan, A. R., et al. (2024). "Microstructure, Mechanical Properties and Corrosion Performance of Laser-Welded NiTi Shape Memory Alloy in Simulated Body Fluid." Materials, 17(19), 4801.
[15] Delobelle V, Favier D, and Louche H 2013 Heat estimation of infrared measurement compared to the DSC for austenite to R phase transformation in a NiTi alloy. *J. Mater. Eng. Perform*. **22(6)**: 1688–1693.
[16] Zoeram A.S and Mohsenifar F 2016 Effect of welding speed on mechanical and fracture behavior of Nitinol laser–joints. *Weld. World*. **60(1)**: 11–19.
[17] Oliveira J.P, Miranda R.M and Fernandes F.B 2017 Welding and joining of NiTi shape memory alloys: a review. *Prog. Mater. Sci*. **88**: 412–466.

[18] Zeng Z, Oliveira J.P, Ao S, Zhang W, Cui J, Yan S and Peng B 2020 Fabrication and characterization of a novel bionic manipulator using a laser processed NiTi shape memory alloy. *Opt Laser Technol*. **122**: 105876.
[19] Falvo A, Furgiuele F.M and Maletta C 2005 Laser welding of a NiTi alloy: Mechanical and shape memory behaviour. *Mater. Sci. Eng. A.* **412(1–2)**: 235–240.
[20] Oliveira J.P, Barbosa D, Fernandes F.B and Miranda R.M 2016 Tungsten inert gas (TIG) welding of Ni–rich NiTi plates: functional behavior. *Smart Mater. Struct*. **25(3)**: 03LT01.
[21] Kramár T, Tauer J, and Vondrouš P 2019 Welding of nitinol by selected technologies. *Acta Polyt*. **59(1)**: 42–50.
[22] Prabu S. M, Madhu H. C, Perugu C. S, Akash K, Mithun R, Kumar P. A & Palani I. A 2019 Shape memory effects temperature distribution and mechanical properties of friction stir welded NiTinol. *J. Alloys Compd*. **776**: 334–345.
[23] Datta S, Bhattacharjee R, and Biswas P 2023 Present status and future trend of friction stir–based fabrication of NiTinol: a review. *Weld World **67*(2)**: 269–307.
[24] Li Chunjie, Sansan Ao, J. P. Oliveira, Mingpeng Cheng, Zhi Zeng, Huijie Cui, and Zhen Luo 2020 Ultrasonic spot welded NiTi joints using an aluminum interlayer: Microstructure and mechanical behavior. *J. Manuf. Process. **56***: 1201–1210.
[25] Resnina N, Palani I A, Belyaev S, Prabu S M, Liulchak P, Karaseva U, Manikandan M, Jayachandran S, Bryukhanova V, Sahu A, and Bikbaev R 2021 Structure, martensitic transformations, and mechanical behavior of NiTi shape memory alloy produced by wire arc additive manufacturing. J. Alloys Compd. **851**: 156851.
[26] Manoj S.R and Bharathi K.T.D 2021 Effect of heat input and post weld heat treatment on the phase transformation temperature of TIG–welded nitinol sheets. *Surf. Rev. Lett.* **28(12)**: 1–9.
[27] Saha P, Datta S, Raza M.S, and Pratihar D.K 2019 Effects of heat input on weld–bead geometry, surface chemical composition, corrosion behavior and thermal properties of fiber laser–welded Nitinol shape memory alloy. *J. Mater. Eng. Perform.* **28(5)**: 2754–2763.
[28] Datta S, Raza M.S, Saha P and Pratihar D.K 2019 Effects of process parameters on the quality aspects of weld–bead in laser welding of NiTinol sheets. *Mater. Manuf. Process*. **34(6)**: 648–659.
[29] Jianwen Wu, Mengjia Xu, Sanbao Lin, Qin Zhang, Xiangmiao Wu, Jiyu Tian and Zhenmin Wang 2023 Refining microstructures and enhancing mechanical properties of Inconel 718 weldment via fast–frequency double pulsed waveforms adopting in FFP–TIG. *J.Mater Process.Technol*. **314**: 117882.
[30] Xuejun Sun, Bojin Qi, Zihao Jiang, Caiyou Zeng, and Baoqiang Cong 2022 Refined weld microstructure and enhanced joint mechanical property of 1460 Al–Li alloys via double–pulsed variable polarity TIG arc welding. *J. Manuf. Process.* **82**: 738–749.
[31] Zhenmin Wang, Zixiao Gui, Jianwen Wu, Qin Zhang, Xiangmiao Wu, Sanbao Lin and Jiyu Tian 2023 Microstructure and high–temperature mechanical properties of Inconel 718 superalloy weldment affected by fast–frequency pulsed TIG welding. *J. Manuf. Process.* **89**: 338–342.
[32] Parimanik S R, Mahapatra T R, Mishra D, and Rout A.K, 2023. Optimisation of performance characteristics in laser welding of Nitinol wires using Taguchi and grey relation analysis. *Adv. Mater. Process. **9*(1)**: 186–195.
[33] Mehrpouya M, Gisario A and Elahinia M 2018 Laser welding of NiTi shape memory alloy: *A review. J. Manuf. Process.* **31**: 162–186.
[34] Parimanik S R, Mahapatra T R, and Mishra D 2023. A systematic literature review on laser welding of NiTi SMA. *Lasers Manuf. Mater. Process. **10*(1)**: 77–117.
[35] A. Ikai, K. Kimura, and H. Tobushi 1996 TIG welding and shape memory effect of TiNi shape memory alloy. *J Intell Master Syst Struct.* **7(6)**: 646–655.
[36] Min Hong, Shalin Wang, Wenjun Sun, Jijun Xin, and Liming Ke 2022 Effect of welding speed on microstructure and mechanical properties of selective laser melting Inconel 625 alloy laser welded joint. *J. Mater. Res. Technol.* **19**: 2093–2103.
[37] Costa J D de Sousa, M B, Fook, N.C.M.L, Alves, J.J.N, de Araújo, C.J, Prasad S, Campos, A.R.N., and de Santana, R.A.C., 2016 Obtaining and characterization of Ni–Ti/Ti–Mo joints welded by TIG process. *Vacuum*. **133**: 58–69.
[38] Tam B, Pequegnat A, M. I. Khan, and Zhou Y 2012 Resistance micro-welding of Ti–55.8 wt pct Ni nitinol wires and the effects of pseudoelasticity *Metall Mater Trans A: Phy Metall Mater Sci.* **43**: 2969–2978.
Shashikala A, Muniraju M, and Pakkirappa H 2023. Experimental investigation of rotary friction welding on the mechanical properties of NiTinol alloy. *Weld. Int. **37*(4)**: 163–173.
[39] Wang Y, Li H, Li Z, Zhang Y, Qin J, Chen G, Qi B, Zeng C, and Cong B 2023 Refining microstructure of medium–thick AA2219 aluminium alloy welded joint by ultrasonic frequency double–pulsed arc. *J. Mater. Res. Technol.* **23**: 3048–3061.
[40] Mwangi J W, Nguyen L T, Bui, V.D, Berger T, Zeidler H, and Schubert A , 2019. Nitinol manufacturing and micromachining: A review of processes and their suitability in processing medical–grade nitinol. *J. Manuf. Process.* **38**: 355–369.

[41] Shantharaj M, Rajasekaran T, and Pandey C, 2023. Effect of process parameters on double pulse metal inert gas welded joints of Inconel 718 superalloy. *Weld World* **67(11)**: 2477–2492.